Probabilistic electrical resistivity tomography of a CO_2 sequestration analog

Tobias Lochbühler[1*], Stephen J. Breen[2,3], Russell L. Detwiler[2], Jasper A. Vrugt[2,4], Niklas Linde[1]

[1] Applied and Environmental Geophysics Group, Institute of Earth Sciences, Faculty of Geosciences and Environment, University of Lausanne, Lausanne, Switzerland

[2] Department of Civil and Environmental Engineering, University of California Irvine, Irvine, CA, USA

[3] now at Department of Earth and Planetary Science, University of California Berkeley, Berkeley, CA, USA

[4] Department of Earth System Science, University of California Irvine, Irvine, CA, USA

*corresponding author: Tobias.Lochbuehler@unil.ch

Abstract

Electrical resistivity tomography (ERT) is a well-established method for geophysical characterization and has shown potential for monitoring geologic CO_2 sequestration, due to its sensitivity to electrical resistivity contrasts generated by liquid/gas saturation variability. In contrast to deterministic inversion approaches, probabilistic

inversion provides the full posterior probability density function of the saturation field and accounts for the uncertainties inherent in the petrophysical parameters relating the resistivity to saturation. In this study, the data are from benchtop ERT experiments conducted during gas injection into a quasi-2D brine-saturated sand chamber with a packing that mimics a simple anticlinal geological reservoir. The saturation fields are estimated by Markov chain Monte Carlo inversion of the measured data and compared to independent saturation measurements from light transmission through the chamber. Different model parameterizations are evaluated in terms of the recovered saturation and petrophysical parameter values. The saturation field is parameterized (1) in cartesian coordinates, (2) by means of its discrete cosine transform coefficients, and (3) by fixed saturation values in structural elements whose shape and location is assumed known or represented by an arbitrary Gaussian bell structure. Results show that the estimated saturation fields are in overall agreement with saturations measured by light transmission, but differ strongly in terms of parameter estimates, parameter uncertainties and computational intensity. Discretization in the frequency domain (as in the discrete cosine transform parameterization) provides more accurate models at a lower computational cost compared to spatially discretized (cartesian) models. *A priori* knowledge about the expected geologic structures allows for non-discretized model descriptions with markedly reduced degrees of freedom. Constraining the solutions to the known injected gas volume improved estimates of saturation and parameter values of the petrophysical relationship.

1 Introduction

Geophysical monitoring of subsurface processes is a requirement for the effective management of hydrocarbon and geothermal resources, and to assess the integrity of storage units for sequestrated CO_2 or nuclear waste (e.g., San Andres and Pedersen, 1993; Li, 2003; Chadwick et al., 2005; Orange et al., 2009; Bhuyian et al., 2012). Adequate monitoring tools provide time-lapse data that allow changes in subsurface properties to be detected and analyzed. Recovering the subsurface properties involves geophysical inversion, that is, the inference of a set of model parameters $\mathbf{m}$ from a set of data $\mathbf{d}$. In this study, the focus is on geophysical monitoring of geologic CO_2 sequestration, where electrical resistivity tomography (ERT) has shown great potential (Christensen et al., 2006; Nakatsuka et al., 2010; al Hagrey, 2011; al Hagrey et al., 2013; Bergmann et al., 2012; Carrigan et al., 2013; Doetsch et al., 2013). The benefits of ERT arise from the sensitivity of electrical resistivity upon liquid/gas saturation and from well-established and cost-efficient techniques for sensor installations at the surface and within boreholes (Ramirez et al., 2003; Slater et al., 2000).

Inverse problems can be tackled deterministically (e.g., Menke, 1989) or probabilistically (e.g., Tarantola, 2005). We herein use a probabilistic approach, namely Markov chain Monte Carlo (MCMC) sampling of the posterior probability density function (pdf) (Mosegaard and Tarantola, 1995; Sambridge and Mosegaard, 2002). Obtaining a full marginal pdf for each model parameter is especially beneficial when the interest is not solely on the estimated parameter value itself but also on its uncertainty. If, for example,

the objective is to locate possible leakage of injected CO_2, one single model as obtained by deterministic inversion is not enough to assess the risk that leakage takes place.

Geophysical inversion results are dependent on the entire modeling process, including the formulation and accuracy of the forward problem, the data quality and processing, and the formulation and parameterization of the inverse problem. Adequate analysis of these possible sources of error and bias is an active field of research (e.g., Ory and Pratt, 1995; Trampert and Snieder, 1996; Scales and Tenorio, 2001; Kalscheuer and Pedersen, 2007; Hansen et al., 2014). A better understanding of these error sources will improve the resulting inverse models or at least help to better characterize model resolution and uncertainty. In this study, we probabilistically invert ERT data to recover the spatial saturation field in 2D. While the forward formulation and the data remain unchanged, the inversions are repeated for different parameterizations of the spatial water saturation distribution. This allows us to highlight benefits and limitations of different model parameterizations in terms of the estimates of the saturation field and petrophysical parameters, as well as their computational requirements and dependence on additional information.

This research builds on the work by Breen et al. (2012). They recorded time-lapse ERT data for a brine-saturated sand chamber during injection of air, a reasonable surrogate for supercritical CO_2. The sand was arranged to mimic a geologic formation targeted for CO_2 storage in the form of an anticlinal trap, the sand chamber can thus be seen as a reservoir analog. They inverted for resistivity models using standard smoothness-constrained deterministic inversion before translating them into saturation models as-

suming a known petrophysical relation. The resulting 2D saturation models were compared to high-resolution saturation images obtained with a CCD (charge-coupled device) camera. These ERT data are here inverted within a probabilistic framework and the obtained models are compared to the inversion results and the CCD images by Breen et al. (2012).

The ERT data were acquired in a laboratory environment, which constitutes a compromise between data from real field experiments and data from entirely numerical studies. Unlike synthetic data, the available lab data allow investigating measurement-related issues and possible model bias, since synthetic data are usually contaminated with zero-mean random noise only. At the same time, the laboratory environment provides full control and knowledge of the underlying 'geology' and the resulting saturation field which enables a detailed quality assessment of the inverse models. Examples of recent bench-scale analogs of ERT monitoring experiments include the work of Wagner et al. (2012) and Pollock and Cirpka (2012).

2 Methods

2.1 The Forward Problem

The principle of ERT surveys is the sequential injection of electrical currents between many pairs of electrodes distributed on the surface or within boreholes. Simultaneously, resulting potential differences away from the injection pairs are measured across other electrode pairs in the array. These voltages are a function of the local electrical resis-

tivity distribution (unknown), the source current magnitude (known), and the electrode geometries (known). The forward problem in ERT thus consists of calculating the electrical potential differences for all pairs of measurement and current injection electrodes for a given resistivity model, where the electrodes are considered as point-electrodes. This involves solving Poisson's equation for the electrical potential, here performed on a finite difference grid (Binley and Kemna, 2005).

The two experimental relations of Archie (1942) provide a petrophysical link between the bulk resistivity field $\boldsymbol{\rho}$ and the spatial distribution of fluid saturation $\mathbf{S}_w$ for partially saturated porous media:

$$\boldsymbol{\rho} = \rho_w \, \varphi^{-m} \, \mathbf{S}_w^{-n}, \tag{1}$$

where ρ_w is the resistivity of the pore fluid (here, water), φ is the porosity, m and n are the cementation and saturation exponents, respectively. The dimensions of $\boldsymbol{\rho}$ and $\mathbf{S}_w$ are given by $N_x \times N_z$, with N_x and N_z being the grid dimensions. Equation (1) is valid when φ, m and n are constant throughout the domain and when surface conductivity is ignored (Waxman and Smits, 2003). Replacing φ^{-m} by the formation factor F yields

$$\boldsymbol{\rho} = \rho_w \, F \, \mathbf{S}_w^{-n}. \tag{2}$$

The product $\rho_w \, F$ is the bulk resistivity at full saturation, often referred to as ρ_b. The basic assumption behind this relationship is that all resistivity changes are related to changes in saturation. This means that at full saturation $\boldsymbol{\rho} = \rho_b \, \mathbf{1}_{N_x \times N_z}$, where $\mathbf{1}$ is a matrix filled with ones. Simultaneous estimation of ρ_b and n allows inverting for $\mathbf{S}_w$

directly. The model vector is then

$$\mathbf{m} = \{\mathbf{S}_w, \rho_b, n\} \tag{3}$$

of dimension $N_x \times N_z + 2$ and the forward problem is

$$\mathbf{d} = g(\mathbf{m}) + \boldsymbol{\varepsilon}, \tag{4}$$

where $g(\mathbf{m})$ is the forward response of $\mathbf{m}$ and $\boldsymbol{\varepsilon}$ is an error term summarizing all measurement and modeling errors.

2.2 Experimental Setup

A full description of the experiment and the measurement system is given by Breen et al. (2012). We only summarize the main elements of the experimental setup here (see also Figure 1).

A translucent sand chamber with dimensions of 57 cm height × 28 cm width × 1 cm depth was constructed to allow for measurement of saturation with ERT and light transmission concurrently. Along both long sides, twenty-one stainless steel electrodes were inserted 2-3 mm into the sand, through a non-conducting plastic gasket. The chamber was filled with two quartz sands of different sizes (d_{50} of 0.29 mm and 0.53 mm), with finer on top. Micro-layering was generated within each layer by pouring the sand through a series of screens in discrete intervals, with the intention of mimicking a typical sedimentary formation. The sand-filled chamber was mounted vertically in front of a uniform, well-controlled light source. A 12-bit CCD camera took images of the sand chamber with its focal plane 1.5 m away, yielding a pixel resolution of 0.2 mm × 0.2 mm.

Saturation fields were calculated from grayscale pixel intensities using a well-established method proposed by Tidwell and Glass (1994) and further developed by Niemet and Selker (2001).

In a single ERT scan, the data acquisition system generated 1,536 four-pole data points, predominantly in a rotating dipole-dipole orientation. The sand/fluid system was held in steady state between injections for the ERT scan, which took approximately eight minutes. ERT data were inverted according to the deterministic Occam's inversion methodology (Constable et al., 1987), with a differencing scheme to improve the performance of time-lapse inversion (LaBrecque and Yang, 2001). Archie's 2nd law was used with *a priori* estimates of parameter values to convert resistivity to saturation. The background fluid was a potassium-chloride solution with 1.6 Ωm resistivity, similar to brine found in CO_2 sequestration reservoirs. Because the translucent sand chamber is unable to withstand reservoir pressures and temperatures, air was used as a resistive, non-wetting surrogate for supercritical CO_2. The air was injected at 1 ml/min from a small tube near the bottom of the chamber and allowed to migrate buoyantly toward the fine sand barrier, where a plume developed over time. In this study, we evaluate a representative ERT data set taken after 28 ml had been injected.

[Figure 1 about here.]

2.3 Markov Chain Monte Carlo Inversion

In probabilistic inversions, the space of possible models is randomly sampled. The objective is to find an ensemble of models that are in agreement with the observed data

and with available *a priori* information. The probability of a model to be part of the posterior ensemble, $p(\mathbf{m}|\mathbf{d})$, is given by Bayes rule (e.g., Tarantola, 2005)

$$p(\mathbf{m}|\mathbf{d}) = c\, p(\mathbf{m}) p(\mathbf{d}|\mathbf{m}), \tag{5}$$

where c is a normalization constant, $p(\mathbf{m})$ is the prior distribution and $p(\mathbf{d}|\mathbf{m}) \equiv L(\mathbf{m}|\mathbf{d})$ is the likelihood function. The prior quantifies the probability of a model based on *a priori* knowledge about the model that is independent of the data. This includes knowledge about expected parameter ranges, the shape of the parameter distributions, or expected model morphologies (e.g., Mariethoz et al., 2010; Hansen et al., 2012). The likelihood term describes the probability that the observed data are a result of a proposed model, it is thus a function of the data misfit between observed data, $\mathbf{d}$, and the data predicted by the model, $\mathbf{d}^{\text{pred}}$. If we assume that the data residuals are uncorrelated and normally distributed, the likelihood function, $L(\mathbf{m}|\mathbf{d})$, is given by

$$L(\mathbf{m}|\mathbf{d}) = \prod_{i=1}^{N} \frac{1}{\sqrt{2\pi\sigma_i^2}} \exp\left[-\frac{1}{2}\frac{(d_i^{\text{pred}}(\mathbf{m}) - d_i)^2}{\sigma_i^2}\right], \tag{6}$$

where N is the number of data points and σ_i denotes the standard deviation of the i-th data point.

Metropolis sampling (Metropolis et al., 1953) offers a means to efficiently explore the posterior pdf, since regions in the solution space with high posterior probability are sampled with a higher frequency than regions of low probability. If proposal states are drawn from uniform prior distributions as we do herein, the probability of accepting a proposed model, $\mathbf{m}_{\text{prop}}$, and moving away from the present model state, $\mathbf{m}$, is given by

(Mosegaard and Tarantola, 1995)

$$\alpha = \min\left\{1, \frac{L(\mathbf{m}_{\text{prop}}|\mathbf{d})}{L(\mathbf{m}|\mathbf{d})}\right\}. \tag{7}$$

Generation of a new model state $\mathbf{m}_{\text{prop}}$ requires perturbation of the present state $\mathbf{m}$. The magnitude and the type of perturbation, which signifies the step in the random walk, strongly controls the performance of MCMC sampling. While large perturbations potentially sample the entire solution space, convergence can be slow. Small perturbations promise faster convergence, but risk missing possible solutions and getting stuck in local optima (e.g., Gelman and Rubin, 1992). For low dimensional problems, the model update can be based on adding random perturbations to each individual parameter (e.g., Metropolis et al., 1953). In applied geophysics, the dimensionality of the inverse problem is usually rather high since we are interested in spatially distributed property values. A means to perturb the present model state in high dimensions is the geostatistical approach, where groups of randomly distributed cells or blocks of cells are resimulated in each iteration while honoring the underlying geostatistical spatial dependencies (Mariethoz et al., 2010; Hansen et al., 2012; Cordua et al., 2012). This method, however, requires explicit knowledge about the expected two- or multiple-point statistical relations and the geostatistical simulations can be CPU-expensive.

An alternative way to tackle high dimensional MCMC problems is to store past model states in an archive and to generate new states by recombination of old ones. This is the basic idea of the DREAM$_{(\text{ZS})}$ algorithm (Vrugt et al., 2008; ter Braak and Vrugt, 2008; Vrugt et al., 2009), which has been enhanced with multi-try sampling to simultaneously

create multiple different proposals in each chain and thus to speed up the search efficiency on a distributed computing network (MT-DREAM$_{(\mathrm{ZS})}$, Laloy and Vrugt, 2012). MT-DREAM$_{(\mathrm{ZS})}$ has been successfully used to estimate hundreds of independent parameters (Laloy and Vrugt, 2012; Rosas-Carbajal et al., 2014). In the algorithm, K ($K > 2$) chains are run in parallel and proposals in each chain are generated by adding to the present state the difference of two or more past states sampled from an archive. Furthermore, subspace sampling is implemented, where the choice of updated dimensions (indexed j in Equation 8) is based on a geometric series of crossover values and bounded between 1 and the dimensionality D. A proposal jump within the i-th chain is then

$$\mathbf{\Delta}_j^i = (\mathbf{1}_{D'} + \mathbf{e})\gamma(D')[\mathbf{z}_j^{r1} - \mathbf{z}_j^{r2}] + \boldsymbol{\epsilon}, \tag{8}$$

where D' is the number of updated dimensions, $\mathbf{1}_{D'}$ is a unit vector of dimension D' and $\mathbf{z}_j^{r1}$ and $\mathbf{z}_j^{r2}$ ($r1 \neq r2 \neq i$) are samples from the archive of old states, $\mathbf{Z}$. Ergodicity is ensured by $\mathbf{e} \sim \mathcal{U}_{D'}(-b, b)$ and $\boldsymbol{\epsilon} \sim \mathcal{N}_{D'}(0, b^*)$, where b and b^* are small compared to the width of the target distribution. Based on Random Walk Metropolis, the jump rate gamma is derived from $\gamma(D') = 2.4/\sqrt{2D'}$, but periodically set to one to enable sampling of disconnected posterior modes. For all elements of D unequal to j, $\mathbf{\Delta}^i = 0$. The proposal state is then calculated using

$$\mathbf{m}_{\mathrm{prop}}^i = \mathbf{m}^i + \mathbf{\Delta}^i, \tag{9}$$

where $\mathbf{m}^i$ denotes the present state of the i-th Markov chain. For a detailed description of the algorithm and the algorithmic parameters we refer to Laloy and Vrugt (2012).

To assess whether the algorithm has converged, we use the convergence diagnostics

presented by Gelman and Rubin (1992), where the change of certain characteristics of the target distribution is monitored within a chain and across parallel chains. As proposed by the authors, convergence is assumed to be reached when the $\hat{R}$-value (see original publication) is below a value of 1.2.

2.4 Error Description

Since the purpose of this paper is to analyze possible errors related to the model parameterization, we seek to reduce all other error sources. To do so, we separated the error term in Equation (4), $\boldsymbol{\varepsilon}$, into a part that is systematic, $\boldsymbol{\varepsilon}_{\text{sys}}$, and a part that depends on the modeling, the setting and that includes any random error, $\boldsymbol{\varepsilon}_l$. The systematic error $\boldsymbol{\varepsilon}_{\text{sys}}$ contains all errors independent of saturation, parameterization and repetition. They will repeat in each inversion run, for example, measurement bias due to damaged electrodes, errors due to inaccuracies in the forward problem or numerical errors. The second error term, $\boldsymbol{\varepsilon}_l$, describes errors related to the saturation, to the model parameterization and all random measurement errors. This error will change in each inversion run. We can then rewrite the forward problem

$$\mathbf{d} = g(\mathbf{m}_l) + \boldsymbol{\varepsilon}_{\text{sys}} + \boldsymbol{\varepsilon}_l, \tag{10}$$

where l is a case index.

In a preliminary inversion, we calculated the posterior distribution of the uniform background resistivity when the chamber is entirely water saturated. This is a well-posed problem since we use all 1,536 data to estimate only one parameter, and its distribution is therefore very narrow. From this posterior, we extract the mean background resistivity,

$\overline{\rho}_b$ (which is an estimate of ρ_b), and its standard deviation, σ_{ρ_b}. Adjusting Equation (10) to the saturated, uniform case (indexed *sat*) yields

$$\mathbf{d}_{sat} = g(\rho_b) + \boldsymbol{\varepsilon}_{\mathrm{sys}} + \boldsymbol{\varepsilon}_{\mathrm{sat}}, \tag{11}$$

where the data residuals are (e.g., LaBrecque and Yang, 2001; Doetsch et al., 2010)

$$\mathbf{r} = \mathbf{d}_{\mathrm{sat}} - g(\rho_b) = \boldsymbol{\varepsilon}_{\mathrm{sys}} + \boldsymbol{\varepsilon}_{\mathrm{sat}}. \tag{12}$$

In subsequent inversion runs, we do not invert for $\mathbf{d}$, but for $\mathbf{d}' = \mathbf{d} - \mathbf{r}$ so that Equation (10) becomes

$$\mathbf{d}' = g(\mathbf{m}_l) + (\boldsymbol{\varepsilon}_l - \boldsymbol{\varepsilon}_{\mathrm{sat}}), \tag{13}$$

where $\boldsymbol{\varepsilon}_{\mathrm{sys}}$ is eliminated.

2.5 Model Parameterization

Geophysical forward problems are typically solved by approximate numerical formulations on finite element or finite difference grids. The model is parameterized by grid cells at a discretization that depends on the desired resolution and the available computational resources. In inverse modeling, the parameterization is typically identical to that of the forward problem. This is not a necessity. In many cases it is computationally beneficial to reduce the number of model parameters in the inverse model. Reduction of the model dimensions is particularly important for Bayesian inversion, since with growing number of free parameters the solution space becomes increasingly void and MCMC sampling very inefficient (Curtis and Lomax, 2001).

Models can be represented by an expansion of base functions such that (e.g., Sambridge et al., 2013; Linde, 2014)

$$m(\mathbf{x}) = \sum_{i=1}^{k} m_i \phi_i(\mathbf{x}), \tag{14}$$

meaning that the model m at location $\mathbf{x}$ is given by the coefficients m_i, where i denotes the parameter index, and the base functions ϕ_i. In a cartesian parameterization, for example, ϕ_i are boxcar functions (or, polynomials of degree zero) that are one at the i-th cell and zero elsewhere and m_i are the parameter values. Base function parameterizations require spatial or spectral discretization of the model space so that the discretized units are weighted by their coefficients m_i. Their potential in terms of model space reduction is thus limited if an adequate resolution is to be maintained. Generally, no prior information is needed about expected structures to formulate such parameterizations.

Alternatively, models can be parameterized by objects of fixed or arbitrary shape and size (e.g., Ramirez et al., 2005). Such non-discretized, 'object-based' parameterizations allow for very sparse parameter spaces, but require at least some prior knowledge about the expected geological structures. In this study, we use localized (cartesian) and frequency-based base functions, as well as two kinds of object-based parameterizations.

The free parameters in this study are the parameters that define the saturation field $\mathbf{S}_w$, the background resistivity ρ_b, the saturation exponent n and the relative error level σ_{rel} where $\sigma_{\text{rel}}\, d_i = \sigma_i$. The chamber is discretized by 91×44 cells, which corresponds to a cell size of about 0.6 cm in both directions. Note that even though the model is discretized and parameterized in different ways in this study, it is always retransformed

to this fine cartesian grid before the forward problem is solved.

To allow for the widest possible uncertainties, we assume uniform prior distributions for all parameters. This means that each parameter value is equally probable *a priori* within its respective range. The saturation parameters depend on the model parameterization, as described below. In cases where we directly invert for saturation values, these are assumed to follow a uniform distribution between 0.1 and 1. The distribution of the background resistivity is approximately known from preliminary inversion (see previous section), and it is kept a free parameter allowed to vary within the interval $[\overline{\rho}_b - 3\,\sigma_{\rho_b}, \overline{\rho}_b + 3\,\sigma_{\rho_b}]$. The saturation exponent n is sampled between 1 and 3 (e.g., Donaldson and Siddiqui, 1989; Suman and Knight, 1997). The relative error level σ_{rel} is assumed to follow a Jeffreys prior (Tarantola, 2005), with range between 0.25 and 10 %. Thus, the error levels are distributed uniformly on a logarithmic scale between these bounds. Estimating the measurement errors amounts to hierarchical Bayesian inference (e.g., Malinverno and Briggs, 2004; Bodin et al., 2012).

2.5.1 Cartesian Parameterization

A simple way to reduce the parameter space of the inverse model is to coarsen the grid of the forward problem. Here, we represent the saturation field by a regular grid of 19×9 rectangular cells, thus reducing the model space from 4,004 to 171 parameters. To solve the forward problem, the coarse grid is linearly interpolated to the uncoarsened, fine grid. Despite the relatively coarse discretization, the number of parameters is still sufficiently large to be challenging for MCMC simulation. Note that for probabilistic inversions using

cartesian parameters the effective number of degrees of freedom is typically reduced by regularization (e.g., Rosas-Carbajal et al., 2014) or by the use of constrained priors (e.g., Hansen et al., 2012) to maintain an acceptable CPU-intensity.

[Figure 2 about here.]

2.5.2 Discrete Cosine Transform

The use of orthogonal base functions in the frequency-amplitude domain and their coefficients is becoming increasingly popular in geophysics to represent fields of spatially distributed properties (e.g., Jafarpour, 2011; Linde and Vrugt, 2013). Base functions such as the wavelet or the cosine transform exploit the spatial correlation between subsurface properties which allows for efficient model space compression. For instance, a subsurface with constant or gradually varying properties is adequately represented with just a few terms of an appropriate base function. Many different base functions have been developed and applied to particular problems, mainly in the field of image processing. In geophysics, the most widely used functions are the discrete cosine transform (DCT, Jafarpour et al., 2009, 2010; Linde and Vrugt, 2013) and the wavelet transform (e.g., Jafarpour, 2011; Davis and Li, 2011). Model compression is performed by setting the coefficients of the base function terms beyond a certain threshold equal to zero. The choice of this threshold level is a trade-off between the desired resolution and the dimensionality of the model parameter space. If strong prior information on the expected model structures is available, compression can be based on determination of dominant (most informative) transform coefficients (Jafarpour et al., 2009; Jafarpour, 2011). Without

prior information, the typical procedure is to truncate the high-frequency terms of the corresponding transform and to maintain a fixed number of low-frequency terms (e.g., Linde and Vrugt, 2013). In this study, we use the DCT. This approach exhibits superior compression power over the wavelet transform as its base functions are not spatially localized.

For a uniformly discretized saturation model $\mathbf{S} \in \mathbb{R}^{N_x \times N_z}$, the DCT-II representation in 2D is given by (Ahmed et al., 1974)

$$B(k_x, k_z) = \alpha_{k_x} \alpha_{k_z} \sum_{x=0}^{N_x-1} \sum_{z=0}^{N_z-1} S(x, z) \cos \frac{\pi(2x+1)k_x}{2N_x} \cos \frac{\pi(2z+1)k_z}{2N_z}, \tag{15}$$

where

$$\alpha_{k_x} = \begin{cases} \frac{1}{\sqrt{N_x}}, k_x = 0 \\ \sqrt{\frac{2}{N_x}}, 1 \leq k_x \leq N_x - 1 \end{cases}$$

and

$$\alpha_{k_z} = \begin{cases} \frac{1}{\sqrt{N_z}}, k_z = 0 \\ \sqrt{\frac{2}{N_z}}, 1 \leq k_z \leq N_z - 1. \end{cases}$$

where the DCT coefficients in $\mathbf{B}$ constitute the unknown model parameters.

We tested two different choices for truncation of coefficients, with different frequency content in the set of maintained coefficients. In the first case, we kept the $n = 100$ coefficients of a 10×10 box in the low frequency corner of the transform space as free parameters in the inversion, whereas the other coefficients were set to zero and thus discarded (c.f., DCT-A in Figure 2). Given that the original cartesian grid has 4,004 cells, the compression is 97.5%. In the second case, we considered as parameters the 105 low-frequency coefficients arranged in a triangular block of the transform space (c.f.,

DCT-B in Figure 2). This latter choice has the advantage of containing more high-frequency coefficients in the x- and z- direction. Both are reasonable choices when no prior information about the expected frequency content in the inverse models is available. The prior range of the DCT coefficients was chosen such that saturation values in the expected range between 0.1 and 1 can be adequately represented. Random sampling of the DCT coefficients can lead to physically unrealistic saturation values when the individual transform terms are added. We therefore expressed the saturation as

$$\mathbf{S}_w = \text{logit}^{-1}\left(\mathcal{T}_{DCT}^{-1}(\mathbf{B})\right), \tag{16}$$

where $\mathcal{T}_{DCT}^{-1}$ denotes the inverse DCT. The inverse logit-transform ensures that the saturation values stay within physical bounds since the logit-transform $\text{logit}(S_w) = \log\left(\frac{S_w}{1-S_w}\right)$ is only defined for $S_w \in [0, 1]$.

2.5.3 Structural Prior Parameterization

Geological targets subject to monitoring have typically undergone geophysical (seismic) pre-investigations to map the main geological units (al Hagrey et al., 2013). If the main geological structures are known, then a direct parameterization can be used and a pixel- or frequency-based parameterization is unnecessary. We can instead assume the location and the dimensions of the anticlinal geological trap to be known (c.f., 'Structural Prior' in Figure 2). The regions above and below the cap are parameterized as zones of uniform saturation crossed by thin zones that represent possible gas pathways. Within the trap, we estimate the saturation in the cap top, $S_{w,captop}$, and the saturation difference for each row of grid cells in the fine cartesian discretization, $\Delta S_w \geq 0$, such that in each

i-th row, the saturation is

$$S_{w,i} = S_{w,captop} + \sum_{k=1}^{i} \Delta S_{w,k}. \tag{17}$$

This parameterization allows for different saturation gradients within the cap, including constant and zero gradients. By considering only positive values of ΔS_w physically unrealistic saturation gradients are prevented since then S_w is monotonic increasing from the top of the cap to the bottom. This parameterization involves 14 parameters only: the background water saturation above and below the cap structure, the saturation within the pathway zones, the water saturation within the cap top, and the saturation change for the individual model rows within the cap.

2.5.4 Gaussian Bell Parameterization

Geological reservoirs or storage units are often formed by anticlinal trap structures. We can describe the geological interface as a convex 2D shape using a Gaussian bell curve. By shifting the center of the bell's peak horizontally and vertically and by varying the height and the width of the curve, anticlines of arbitrary shape can be represented. The curve is given by

$$f(x) = a \exp\left[-\frac{(x-b)^2}{2c^2}\right] + d, \tag{18}$$

where a, b, c, and d are additional parameters to be estimated jointly with the water saturation above and below the anticline, in the cap top and by the saturation changes within the cap as described in the previous section. In this case the height of the cap is not fixed. We are parameterizing the region within the cap by ten horizontal layers

and invert for the saturation change in each layer. Depending on the height of the cap, the thicknesses of the ten layers are squeezed or stretched and the values of saturation change are projected on the fine grid of the forward problem by linear interpolation.

3 Results

We performed three different inversion series, and ran different trials for all considered model parameterizations. The series are based on the injection experiment by Breen et al. (2012), and the objective is to estimate the saturation field after the injection of 28 ml air. To benchmark the applicability of the methodology presented herein, we first apply our method to synthetically generated data. Then, the method is applied to real data measured by Breen et al. (2012). In all inversions we used the standard settings of the algorithmic parameters of MT-DREAM$_{(\mathrm{ZS})}$ (Laloy and Vrugt, 2012). Three different chains are run jointly in parallel and in each chain five different proposals are created at each iteration and evaluated simultaneously on a distributed computing network to speed up convergence to a limiting distribution. This requires the use of 15 CPUs.

The quality of the inverse saturation models is assessed by comparing the estimated saturation field, $\mathbf{S}_w$ with the reference field $\mathbf{S}_{w,\mathrm{ref}}$, which is the known saturation field in the synthetic study and the saturation field inferred from CCD imaging for the real data studies. We formulate the saturation error, $\mathrm{E}_{\mathrm{sat}}$ as a pixel-by-pixel difference criterion

$$\mathrm{E}_{\mathrm{sat}} = \left\| \frac{1}{\sqrt{N_x N_z}} (\mathbf{S}_w - \mathbf{S}_{w,\mathrm{ref}}) \right\|_2 . \tag{19}$$

As a global criterion for model adequacy, we use the estimated volume of total injected

gas, V_{gas},

$$V_{gas} = V_{\text{tot}}\,\varphi\,(1 - \bar{S}_w), \tag{20}$$

where V_{tot} denotes the total volume of the sand chamber and $\bar{S}_w$ is the mean saturation of all model cells. The porosity φ is assumed to be constant and known *a priori*. Adequate models should provide a gas volume estimate close to the true value of 28 ml.

3.1 Synthetic Study

A synthetic test study was conducted to investigate the effect of different model parameterizations when the true saturation field, the true petrophysical parameters and the actual measurement errors are known. Electrical potential differences were calculated for the saturation field after the 28 ml injection. The saturation was taken from the corresponding CCD image (Figure 3 and Figure 3 (bottom) in Breen et al. (2012)). We defined $\rho_w = 1.6\,\Omega$m, $\varphi = 0.38$, $m = 1.45$ and $n = 2$ and used the petrophysical relation given in Equation (1) to derive the resistivity field for which the forward problem was solved. The synthetic data were contaminated with heteroscedastic Gaussian noise with a standard deviation equal to 0.5 % of the measurement value.

The posterior mean values of the estimated saturation fields are shown in Figure 3. Due to the coarse discretization, the cartesian posterior mean model (Figure 3b) provides a very blocky description of the saturation field. The saturation error (Table 2) is large, indicating that the true saturation cannot be adequately represented by the coarse cartesian parameterization. The estimated saturation fields of the DCT parameterizations feature overly smooth interfaces with small inversion artifacts above and below the

cap. These deviations are a result of the truncation of the DCT representation (Figure 3c-d). The DCT parameterized models are much closer to the true field than the cartesian models, which is also reflected in the 20 to 30 times smaller saturation error (Table 2).

Results from the object-based parameterizations (Figure 3e-f) are visually closer to the true saturation field, due to the use of prior information on the expected structures. They exhibit a similar saturation error as the DCT parameterized models (Table 2). Note that in the case of the Gaussian Bell parameterization the estimated shape and location of the trap is very similar to the true shape imposed by the Structural Prior parameterization. Lower estimated saturation values in the central regions below the cap indicate that there is some sensitivity to the saturation change caused by the gas pathway between injection point and the trap structure.

All parameterizations overestimate the volume of injected gas (Table 2), which is not surprising due to the underestimation of the saturation within the plume. This problem is quite profound for the DCT-B parameterized models, which provide rather poor gas volume estimates of almost 50 ml. On the contrary, for the Structural Prior parameterization the overestimation of the gas volume is negligible (estimates around 30 ml). Detailed prior knowledge about the structural composition of the subsurface thus helped to improve the estimates of this volumetric parameter. The vast differences in the gas volume estimates highlight a strong dependency of the modeling outcome on the choice of the parameterization.

Uncertainties of the estimated saturation values are represented by their standard

deviation of the saturation estimate in each pixel. They are largest in the corners of the cartesian parameterization with maximum values up to 0.4, reflecting low sensitivities in these regions (Figure 3g). The sharper interfaces between high and low saturation for DCT-B compared to DCT-A are accompanied by higher uncertainties (Figure 3c-d and h-i). Considerable saturation uncertainty with values around 0.4 is also associated with the depth of the upper cap boundary in the Gaussian Bell parameterization (Figure 3k). The generally small parameter uncertainties are reflected in the individual posterior realizations with differences between realizations that are very small (Figure 4). This demonstrates that the inverse problem is well-constrained by the relatively large number of data.

Estimated data error levels are higher than the contamination error of 0.5 % and vary between the different parameterizations (Figure 5a-e). Since the parameterization is the only possible error source that differs between the shown cases, these results demonstrate that the parameterization constitutes a significant source of error (Trampert and Snieder, 1996). The error estimates are lowest for the DCT parameterizations (Figure 5b-c) and higher for the object-based parameterizations (Figure 5d-e). Despite owning the most degrees of freedom, the cartesian models exhibit higher data error estimates than the DCT parameterized models. This shows that the coarse grid does not provide a suitable model representation. The bimodal distribution of error level estimates for the Gaussian Bell case is consistent with the presence of two dominant modes of the posterior models with different heights of the cap (c.f., Figure 3k and 4e).

The estimates of the saturation exponent n are close to the true value of 2 for

all parameterizations except for DCT-B (Figure 6a-e). The underestimation of n for this case corresponds well to the clear underestimation of the saturation within the cap, since these parameters values counterbalance each other (c.f., Equation (1)) and produce resistivity models with reasonable data predictions.

As expected, the number of iterations required to reach convergence depends on the dimensionality of the parameter space (Table 1). The lower the number of parameters, the faster the convergence of MT-DREAM(ZS) to a limiting distribution. Indeed, prior information about the subsurface structure used in the object-based parameterization drastically reduces the CPU requirements.

[Figure 3 about here.]

[Figure 4 about here.]

[Figure 5 about here.]

[Figure 6 about here.]

[Table 1 about here.]

[Table 2 about here.]

3.2 Real Data Study

We now present the results for the experimental data measured by Breen et al. (2012). We focus our attention on the saturation data measured after the injection of 28 ml of gas. Breen et al. (2012) presented the results of a deterministic least-squares inversion,

which are used herein for comparative purposes. Figure 7b, taken from Breen et al. (2012), displays the resulting model for the deterministic inversion. This model is overly smooth and features typical inversion artifacts in form of anomalies in the corners of the domain, where the parameter estimates are primarily controlled by the smoothness regularization due to the low sensitivities in these regions. These anomalies are clearly artifacts as they are not detected by the CCD imaging (Figure 7a)

Overall, the resulting models from probabilistic inversion provide a sharper image of the saturation distribution (Figure 7a-g). As in the synthetic study, the cartesian grid is too coarse to adequately represent the gas plume (Figure 7c, Table 2). This demonstrates the limitations of cartesian parameterizations for MCMC inversions. As in the synthetic study, the DCT parameterized models are visually closer to the saturation field derived from CCD imaging and their saturation errors are around 20 times lower than for the cartesian models (Figure 7d-e, Table 2). The DCT-B parameterization allows for somewhat sharper interfaces but exhibits spectral artifacts in the horizontal direction. Both object-based parameterizations produce saturation models with a plume that is slightly smaller than observed in the CCD image (Figure 7f-g). In the case of the Gaussian Bell models, this underestimation of the plume dimensions leads to saturation errors that are about 60 % higher than those of the Structural Prior parameterizations (Table 2).

Parameter uncertainties are generally higher than in the synthetic data study. The uncertainty is largest for the saturation estimates of low-sensitivity cells in the cartesian parameterized models (Figure 7h), in the size of the plume for the DCT-B parameter-

ization (Figure 7j) and in the cells defining the upper boundary of the plume in the Gaussian Bell parameterized models (Figure 7l).

The relative data errors range between 3.5 and 9 % (Figure 5f-j) and are significantly higher than those observed earlier for the synthetic study. With the exception of the cartesian models, the error estimates generally decrease with increasing dimensionality of the parameter space (MacKay, 2003). The estimates of the saturation exponent vary widely between the different parameterizations (Figure 6f-j). High and low estimates (as observed for the DCT-B and the Structural Prior parameterizations) can be explained by under- and overestimation of the saturation within the plume, respectively. Note that the true value of n is unknown for the real data study.

It is worth noting that the results are in general agreement with the findings of the synthetic study. This inspires confidence in the ability of the proposed parameterization and inversion approach to provide reasonable models, even if the true saturation, petrophysics, and modeling errors are unknown.

[Figure 7 about here.]

3.3 Constraining models with the total injected gas volume

In CO_2 storage facilities, the total volume of injected gas is a well-monitored quantity. Assuming that all of the injected gas has been captured in the resolved model domain, this volume provides a strong constraint for the inversion. This assumption is quite realistic in the present case study, as the geometry of the model domain is equivalent to that of the sand chamber. The relationship between the estimated saturation field and

the estimated volume of gas within the system, V_{gas}, is given in Equation (20). This dependency can be imposed as a constraint in two different ways: (i) as a hard constraint, meaning that only models for which $V_{gas} = V_{\text{inj}}$ are drawn as proposal states, where V_{inj} signifies the known volume of injected gas; or (ii) as a soft constraint, where deviations between V_{gas} and V_{inj} are penalized. We adopt (ii), such that a poor agreement can be taken as an indicator that gas has left the domain and that the above-mentioned assumption is violated. We hence treat V_{inj} as an additional observation, and extend the likelihood function to account for differences between the observed, V_{inj}, and simulated, $V_{gas}(\mathbf{m})$, gas volume. The standard deviation of the measured injected gas volume is assumed to be known and equal to 1 % of V_{inj}.

We now discuss the results of this new inversion, which hereafter we refer to as constrained inversion. The explicit use of the injected gas volume in the likelihood function has a positive effect on the inversion results. The resulting posterior means of the saturation estimates are closer to the saturation field retrieved by the CCD image compared to the unconstrained case, in that some of the inversion artifacts in the cartesian and DCT parameterized models are reduced (Figure 8c-e), and saturation within the plume is better represented for the Structural Prior parameterization (Figure 8f). While the saturation errors remain similar to the unconstrained study, the estimated gas volumes are now very close to their true value of 28 ml, with posterior mean estimates ranging between 27.9 and 32.7 ml (Table 2). The estimated uncertainties are generally reduced compared to the unconstrained case, with a particularly strong uncertainty reduction for the DCT parameterizations (Figure 8h-l). Figure 9 shows for the DCT-A parameter-

ization how the distribution of the saturation in the center of the cap structure changes from the prior to the constrained posterior. The prior distribution (light gray) contains saturation values over the entire range between values of 0 and 1. The higher densities close to the bounds is due to the applied logit-transform used to map the sampled DCT coefficients into saturation values. The MCMC inversion of the ERT data yields posterior saturation values which are concentrated around a mean of 0.37 (dark gray). If we constrain the inversion with the measured total volume of injected gas, then the posterior saturation values increase, and reach a mean value of about 0.49 which is very close to the measured saturation value of 0.46 inferred from CCD imaging.

The estimated data error levels are similar to those for the unconstrained case (Figure 5k-o). Large differences in the estimates of this parameter could be an indicator of gas migration out of the model domain, because larger error estimates would suggest a violation of our assumptions regarding the total volume of injected gas. Results for all model parameterizations yield an estimate of the saturation exponent, n of around 2. The gas volume constraint thus clearly helped to obtain a more coherent estimate of this petrophysical parameter as it is similar regardless of the chosen model parameterization (Figure 6k-o).

[Figure 8 about here.]

[Figure 9 about here.]

4 Discussion

We show that probabilistic inversion of ERT data is a feasible approach to monitor geologic storage of CO_2. Unlike deterministic inversions, the probabilistic approach produces an ensemble of possible models that enables assessment of the uncertainty on the model parameter estimates. This information is key to risk assessment and decision making, as it allows for probabilistic analysis of reservoir leakage.

A general problem with sampling in transformed spaces such as the DCT used herein, is that retransformation of the sampled parameters to the original domain often leads to physically unrealistic parameter values due to summation of the transform terms. The inverse logit-transform, when used as shown here, proved a simple but effective tool to ensure that the saturation values produced by retransformation of the sampled DCT coefficients stay within physically realistic bounds. However, the logit-transform is not a linear operator, which means that the DCT coefficients, though sampled from a uniform prior distribution, produce saturation fields that tend to overrepresent values close to the bounds of 0 and 1. In the present case study, this helps to adequately represent the high saturation regions above and below the trap structure, but the inverse models tend to underestimate the saturation within the trap.

The measured ERT data are sensitive to the saturation changes below the trap structure that mark the gas pathway between the injection point and the reservoir. Due to the lower data error level, this feature is detected much clearer in the synthetic case, but nevertheless clearly indicated by the inversions of the real data. Even though

the saturation contrast is rather weak, there is a distinct difference in the saturation above and below the trap. This marks an important improvement compared to Occam's inversion result, for which it is impossible to distinguish the inversion artifact above the cap from the actual feature below the cap (Figures 7 and 8).

The results illustrate to some extent the expectation that the data fit improves with increasing number of model parameters (MacKay, 2003), but this is not a general rule. If the model parameterization is particularly inadequate to represent the subsurface, more model parameters do not necessarily result in models with a reduced data misfit. We observe this for the cartesian parameterization, where the coarse discretization cannot resolve the trap structure in great detail, thereby producing models with comparatively high data misfits.

As in every inverse problem, the choice of the model parameters depends on the type and amount of available data, but also on the goal of the modeling. Since the interest in the present contribution is on the distribution of water saturation, we inverted for saturation values and linked them to resistivities by simultaneously estimating the bulk resistivity under full saturation and the saturation exponent. Alternatively, the fluid resistivity could be assumed known from geophysical logging and the bulk resistivity replaced by the formation factor which then serves as an additional degree of freedom. Explicit inference of the petrophysical parameters allows for careful assessment of the assumed petrophysical model. Unfortunately, poor saturation estimates can be compensated for by poor estimates of the saturation exponent, as encountered in the cartesian and DCT-B parameterizations. This pitfall can be resolved to some extent by imposing

additional constraints on the models as is demonstrated here by applying the gas volume constraint. Similar findings were reported by Laloy et al. (2012) when imaging a tracer plume.

The data inverted in this study were acquired in a quasi-2D sand chamber in a laboratory environment. What implications from these results can be transferred to real-world reservoirs? The general finding that the model parameterization has a strong effect on the required CPU resources and on the fidelity of the inverse models is as valid for a true reservoir as for the analog investigated in this study. Furthermore, adding gas volume constraints on the inverse models will also improve the results if the inverse models are formulated as 3D representations. If the same data are to be inverted using 3D model descriptions, the increase in free parameters and thus the decrease in sampling efficiency differs strongly for the different model parameterizations. The cartesian and DCT parameterized models grow linearly with the number of cells (coefficients) in the y-direction if the same discretization (frequency information) is to be maintained. The object-based parameterizations allow the description of 3D structures with only few additional parameters. If the 3D structure of the geological trap is known, no additional parameters are necessary for the Structural Prior parameterization to represent the saturation distribution in 3D. If the trap is to be described by a 3D Gaussian bell, only two additional parameters (the spread and the lateral shift in y-direction) are required. Given that solving the forward problem in 3D will significantly increase the computational burden, the object-based parameterizations are expected to prove even more beneficial in 3D. Furthermore, it is of general relevance that having an idea about

the structural subsurface composition (as in the Structural Prior parameterized cases) markedly improves the estimates of saturation. This finding supports the results of al Hagrey et al. (2013), who found that the true subsurface resistivity can be reproduced much better if geological unit boundaries are known *a priori* from seismic investigations. As in any probabilistic approach, the prior information must be assessed with care as wrong hypotheses may produce illusive results. The Gaussian Bell parameterization can be seen as a compromise relevant for real-world reservoirs: Possible shapes of geological structures are imposed in the model, but parameter values and the exact locations of the geological interfaces are allowed to vary.

5 Conclusions

In a previous study by Breen et al. (2012), ERT data were measured during injection of air into a brine-saturated quasi-2D sand chamber. We here present the results of probabilistic inversion of these data, using different parameterizations of the saturation field. Object-based parameterizations generally require some prior knowledge about the expected geological structures, but allow description of the saturation fields with relatively few parameters. As an example, we found that the anticlinal trap encountered in this study is well-represented by a Gaussian bell. Concerning the discretized parameterizations used herein, the DCT formulation clearly outperforms classical cartesian formulation of the model parameters in terms of resemblance to the actual saturation field as well as in terms of the inverse models' performance in predicting the measured data. Furthermore, the models can be constrained further if the total volume of injected

gas is included in the likelihood function. This results in much better estimates of the saturation estimates and the saturation exponent.

Acknowledgements

Tobias Lochbühler and Niklas Linde thank the Swiss National Science Foundation (SNF) for funding this research as a contribution to the ENSEMBLE project (grant no. CRSI22_132249). Stephen Breen and Russell Detwiler acknowledge funding from the U.S. Department of Energy, Basic Energy Sciences, Geosciences Program (contract DE-FG02-09ER16003) and Stephen Breen would like to thank Michael Manga and the University of California, Berkeley, Department of Earth and Planetary Science, for support during the completion of this work. Jasper A. Vrugt acknowledges support and funding from the UC-Lab Fees Research Program Award 237285. The MT-DREAM$_{(ZS)}$ code can be obtained from Jasper Vrugt upon request (jasper@uci.edu).

References

Ahmed, N., Natarajan, T., and Rao, K. (1974). Discrete cosine transform. *IEEE Transactions on Computers*, 100(1):90–93.

al Hagrey, S. A. (2011). CO_2 plume modeling in deep saline reservoirs by 2D ERT in boreholes. *The Leading Edge*, 30(1):24–33.

al Hagrey, S. A., Strahser, M., and Rabbel, W. (2013). Seismic and geoelectric modeling

studies of parameters controlling CO_2 geostorage in saline formations. *International Journal of Greenhouse Gas Control*, 19(0):796 – 806.

Archie, G. E. (1942). The electrical resistivity log as an aid in determining some reservoir characteristics. *Trans. AIMe*, 146(99):54–62.

Bergmann, P., Schmidt-Hattenberger, C., Kiessling, D., Rücker, C., Labitzke, T., Henninges, J., Baumann, G., and Schütt, H. (2012). Surface-downhole electrical resistivity tomography applied to monitoring of CO_2 storage at Ketzin, Germany. *Geophysics*, 77(6):B253–B267.

Bhuyian, A. H., Landrø, M., and Johansen, S. E. (2012). 3D CSEM modeling and time-lapse sensitivity analysis for subsurface CO_2 storage. *Geophysics*, 77(5):E343–E355.

Binley, A. and Kemna, A. (2005). DC resistivity and induced polarization methods. In *Hydrogeophysics*, pages 129–156. Springer.

Bodin, T., Sambridge, M., Rawlinson, N., and Arroucau, P. (2012). Transdimensional tomography with unknown data noise. *Geophysical Journal International*, 189(3):1536–1556.

Breen, S. J., Carrigan, C. R., LaBrecque, D. J., and Detwiler, R. L. (2012). Bench-scale experiments to evaluate electrical resistivity tomography as a monitoring tool for geologic CO_2 sequestration. *International Journal of Greenhouse Gas Control*, 9:484–494.

Carrigan, C. R., Yang, X., LaBrecque, D. J., Larsen, D., Freeman, D., Ramirez, A. L.,

Daily, W., Aines, R., Newmark, R., Friedmann, J., et al. (2013). Electrical resistance tomographic monitoring of CO_2 movement in deep geologic reservoirs. *International Journal of Greenhouse Gas Control*, 18:401–408.

Chadwick, R., Arts, R., and Eiken, O. (2005). 4D seismic quantification of a growing CO_2 plume at Sleipner, North Sea. In *Geological Society, London, Petroleum Geology Conference Series*, volume 6, pages 1385–1399. Geological Society of London.

Christensen, N., Sherlock, D., and Dodds, K. (2006). Monitoring CO_2 injection with cross-hole electrical resistivity tomography. *Exploration Geophysics*, 37(1):44–49.

Constable, S., Parker, R., and Constable, C. (1987). Occam's inversion: A practical algorithm for generating smooth models from electromagnetic sounding data. *Geophysics*, 52(3):289–300.

Cordua, K., Hansen, T., and Mosegaard, K. (2012). Monte Carlo full-waveform inversion of crosshole GPR data using multiple-point geostatistical a priori information. *Geophysics*, 77(2):H19–H31.

Curtis, A. and Lomax, A. (2001). Prior information, sampling distributions, and the curse of dimensionality. *Geophysics*, 66(2):372–378.

Davis, K. and Li, Y. (2011). Fast solution of geophysical inversion using adaptive mesh, space-filling curves and wavelet compression. *Geophysical Journal International*, 185(1):157–166.

Doetsch, J., Kowalsky, M. B., Doughty, C., Finsterle, S., Ajo-Franklin, J. B., Carrigan,

C. R., Yang, X., Hovorka, S. D., and Daley, T. M. (2013). Constraining CO_2 simulations by coupled modeling and inversion of electrical resistance and gas composition data. *International Journal of Greenhouse Gas Control*, 18:510–522.

Doetsch, J., Linde, N., and Binley, A. (2010). Structural joint inversion of time-lapse crosshole ERT and GPR traveltime data. *Geophysical Research Letters*, 37(24):L24404.

Donaldson, E. and Siddiqui, T. (1989). Relationship between the Archie saturation exponent and wettability. *SPE Formation Evaluation*, 4(3):359–362.

Gelman, A. and Rubin, D. (1992). Inference from iterative simulation using multiple sequences. *Statistical science*, 7(4):457–472.

Hansen, T., Cordua, K., Jacobsen, B., and Mosegaard, K. (2014). Accounting for imperfect forward modeling in geophysical inverse problems - exemplified for cross hole tomography. *Geophysics*, 79(3):H1–H21.

Hansen, T. M., Cordua, K. S., and Mosegaard, K. (2012). Inverse problems with non-trivial priors: Efficient solution through sequential Gibbs sampling. *Computational Geosciences*, 16(3):593–611.

Jafarpour, B. (2011). Wavelet reconstruction of geologic facies from nonlinear dynamic flow measurements. *Geoscience and Remote Sensing, IEEE Transactions on*, 49(5):1520–1535.

Jafarpour, B., Goyal, V., McLaughlin, D., and Freeman, W. (2009). Transform-domain

721 sparsity regularization for inverse problems in geosciences. *Geophysics*, 74(5):R69–
722 R83.

723 Jafarpour, B., Goyal, V., McLaughlin, D., and Freeman, W. (2010). Compressed his-
724 tory matching: Exploiting transform-domain sparsity for regularization of nonlinear
725 dynamic data integration problems. *Mathematical Geosciences*, 42(1):1–27.

726 Kalscheuer, T. and Pedersen, L. B. (2007). A non-linear truncated SVD variance and
727 resolution analysis of two-dimensional magnetotelluric models. *Geophysical Journal*
728 *International*, 169(2):435–447.

729 LaBrecque, D. J. and Yang, X. (2001). Difference inversion of ERT data: A fast in-
730 version method for 3-D in situ monitoring. *Journal of Environmental & Engineering*
731 *Geophysics*, 6(2):83–89.

732 Laloy, E., Linde, N., and Vrugt, J. A. (2012). Mass conservative three-dimensional water
733 tracer distribution from Markov chain Monte Carlo inversion of time-lapse ground-
734 penetrating radar data. *Water Resources Research*, 48(7):W07510.

735 Laloy, E. and Vrugt, J. (2012). High-dimensional posterior exploration of hydrologic
736 models using multiple-try $DREAM_{(ZS)}$ and high-performance computing. *Water*
737 *Resources Research*, 48(1):W01526.

738 Li, G. (2003). 4D seismic monitoring of CO_2 flood in a thin fractured carbonate reservoir.
739 *The Leading Edge*, 22(7):690–695.

740 Linde, N. (2014). Falsification and corroboration of conceptual hydrological models using
741 geophysical data. *WIREs Water*, 1(2):151–171.

742 Linde, N. and Vrugt, J. A. (2013). Distributed soil moisture from crosshole ground-
743 penetrating radar travel times using stochastic inversion. *Vadose Zone Journal*, 12(1).

744 MacKay, D. J. (2003). *Information theory, inference and learning algorithms*. Cambridge
745 University Press.

746 Malinverno, A. and Briggs, V. A. (2004). Expanded uncertainty quantification in inverse
747 problems: Hierarchical Bayes and empirical Bayes. *Geophysics*, 69(4):1005–1016.

748 Mariethoz, G., Renard, P., and Caers, J. (2010). Bayesian inverse problem and optimiza-
749 tion with iterative spatial resampling. *Water Resources Research*, 46(11):W11530.

750 Menke, W. (1989). *Geophysical data analysis: Discrete inverse theory*, volume 45. Aca-
751 demic Press.

752 Metropolis, N., Rosenbluth, A. W., Rosenbluth, M. N., Teller, A. H., and Teller, E.
753 (1953). Equation of state calculations by fast computing machines. *The Journal of*
754 *Chemical Physics*, 21:1087.

755 Mosegaard, K. and Tarantola, A. (1995). Monte Carlo sampling of solutions to inverse
756 problems. *Journal of Geophysical Research*, 100(B7):12431–12.

757 Nakatsuka, Y., Xue, Z., Garcia, H., and Matsuoka, T. (2010). Experimental study on
758 CO_2 monitoring and quantification of stored CO_2 in saline formations using resistivity
759 measurements. *International Journal of Greenhouse Gas Control*, 4(2):209–216.

760 Niemet, M. R. and Selker, J. S. (2001). A new method for quantification of liquid
761 saturation in 2D translucent porous media systems using light transmission. *Advances*
762 *in Water Resources*, 24(6):651–666.

763 Orange, A., Key, K., and Constable, S. (2009). The feasibility of reservoir monitoring
764 using time-lapse marine CSEM. *Geophysics*, 74(2):F21–F29.

765 Ory, J. and Pratt, R. (1995). Are our parameter estimators biased? The significance of
766 finite-difference regularization operators. *Inverse Problems*, 11:397–424.

767 Pollock, D. and Cirpka, O. (2012). Fully coupled hydrogeophysical inversion of a labo-
768 ratory salt tracer experiment monitored by electrical resistivity tomography. *Water*
769 *Resources Research*, 48(1):W01505.

770 Ramirez, A. L., Newmark, R. L., and Daily, W. D. (2003). Monitoring carbon dioxide
771 floods using electrical resistance tomography (ERT): Sensitivity studies. *Journal of*
772 *Environmental & Engineering Geophysics*, 8(3):187–208.

773 Ramirez, A. L., Nitao, J. J., Hanley, W. G., Aines, R., Glaser, R. E., Sengupta, S. K.,
774 Dyer, K. M., Hickling, T. L., and Daily, W. D. (2005). Stochastic inversion of elec-
775 trical resistivity changes using a Markov Chain Monte Carlo approach. *Journal of*
776 *Geophysical Research*, 110(B2).

777 Rosas-Carbajal, M., Linde, N., Kalscheuer, T., and Vrugt, J. (2014). Two-dimensional
778 probabilistic inversion of plane-wave electromagnetic data: Methodology, model con-

straints and joint inversion with electrical resistivity data. *Geophysical Journal International*, 196(3):1508–1524.

Sambridge, M., Bodin, T., Gallagher, K., and Tkalčić, H. (2013). Transdimensional inference in the geosciences. *Philosophical Transactions of the Royal Society A: Mathematical, Physical and Engineering Sciences*, 371(1984).

Sambridge, M. and Mosegaard, K. (2002). Monte Carlo methods in geophysical inverse problems. *Reviews of Geophysics*, 40(3):1009.

San Andres, R. B. and Pedersen, J. R. (1993). Monitoring the Bulalo geothermal reservoir, Philippines, using precision gravity data. *Geothermics*, 22(5):395–402.

Scales, J. A. and Tenorio, L. (2001). Prior information and uncertainty in inverse problems. *Geophysics*, 66(2):389–397.

Slater, L., Binley, A., Daily, W., and Johnson, R. (2000). Cross-hole electrical imaging of a controlled saline tracer injection. *Journal of Applied Geophysics*, 44(2):85–102.

Suman, R. J. and Knight, R. J. (1997). Effects of pore structure and wettability on the electrical resistivity of partially saturated rocks-a network study. *Geophysics*, 62(4):1151–1162.

Tarantola, A. (2005). *Inverse problem theory and methods for model parameter estimation*. Society for Industrial Mathematics.

ter Braak, C. and Vrugt, J. (2008). Differential Evolution Markov Chain with snooker updater and fewer chains. *Statistics and Computing*, 18(4):435–446.

Tidwell, V. C. and Glass, R. J. (1994). X ray and visible light transmission for laboratory measurement of two-dimensional saturation fields in thin-slab systems. *Water Resources Research*, 30(11):2873–2882.

Trampert, J. and Snieder, R. (1996). Model estimations biased by truncated expansions: Possible artifacts in seismic tomography. *Science*, 271:1257–1260.

Vrugt, J., Ter Braak, C., Clark, M., Hyman, J., and Robinson, B. (2008). Treatment of input uncertainty in hydrologic modeling: Doing hydrology backward with markov chain monte carlo simulation. *Water Resources Research*, 44(12):W00B09.

Vrugt, J., ter Braak, C., Diks, C., Robinson, B., Hyman, J., and Higdon, D. (2009). Accelerating Markov chain Monte Carlo simulation by differential evolution with self-adaptive randomized subspace sampling. *International Journal of Nonlinear Sciences and Numerical Simulation*, 10(3):273–290.

Wagner, F. M., Möller, M., Schmidt-Hattenberger, C., Kempka, T., and Maurer, H. (2012). Monitoring freshwater salinization in analog transport models by time-lapse electrical resistivity tomography. *Journal of Applied Geophysics*, 89:84–95.

Waxman, M. and Smits, L. (2003). Electrical conductivities in oil-bearing shaly sands. *SPE Reprint Series*, pages 107–122.

Figure 1: The fully assembled chamber containing saturated quartz sand, reproduced from Breen et al. (2012). The red square near the bottom of the chamber indicates the gas injection point. Electrode connections can be seen on the left and right sides, and inlet/outlet tubing on top and bottom. The anticlinal transition from the coarser sand on bottom to the finer sand on top was designed to imitate a caprock barrier, while finer layering throughout the chamber imitated natural micro layering in sedimentary formations.

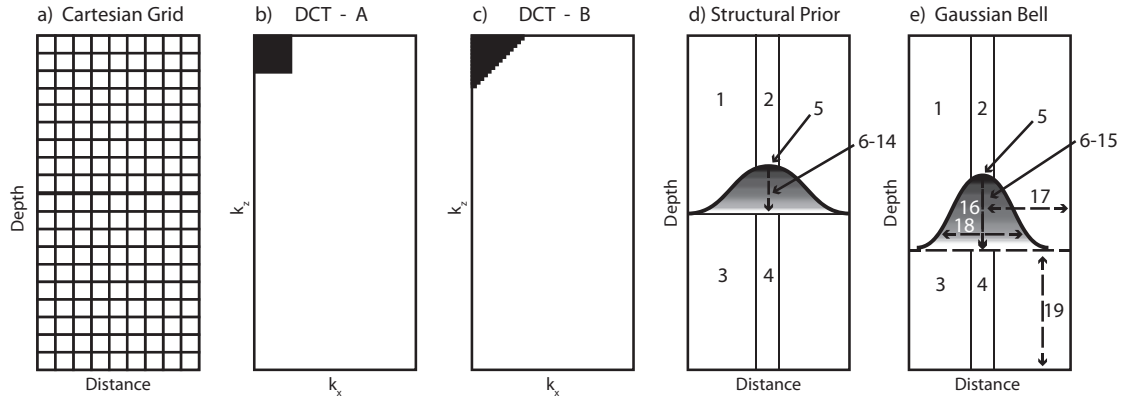

Figure 2: (a-e) Different parameterizations used for inverse modeling. Discrete Cosine Transform is abbreviated by DCT. The enumerated parameters in (d-e) are 1) background water saturation (top), 2) pathway saturation (top), 3) background saturation (bottom), 4) pathway saturation (bottom) 5) water saturation in cap top, 6)-15) saturation change per horizontal layer (one more layer in the Gaussian Bell parameterization), 16)-19) correspond to a, b, c and d in Equation (18).

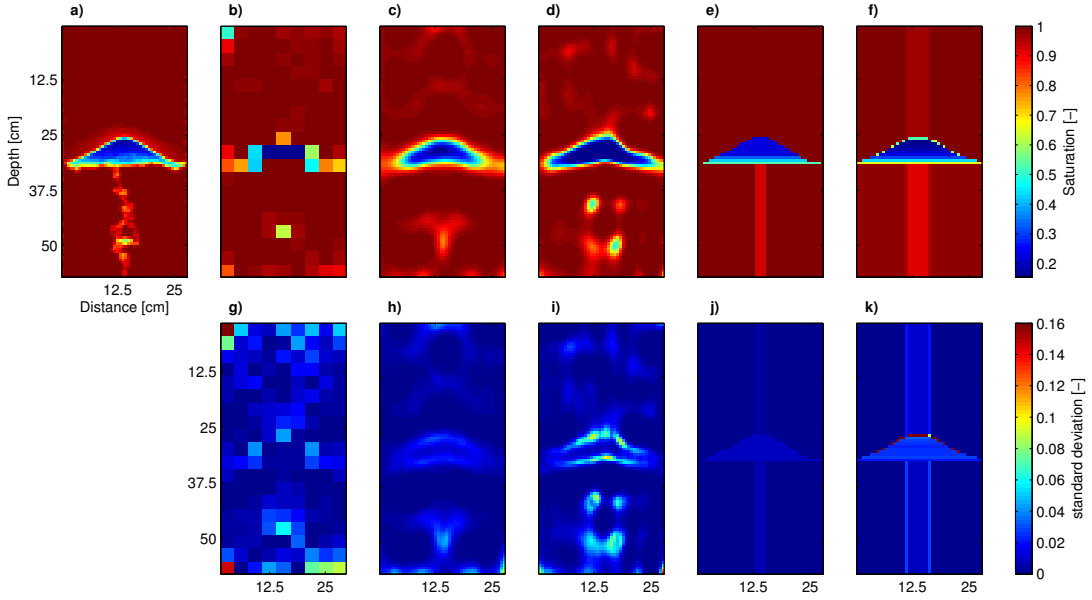

Figure 3: Saturation fields for the synthetic study: a) Saturation from CCD imaging used to calculate synthetic data. (b-f) Posterior mean saturation fields inferred from the MCMC inversion. (g-k) Standard deviations of the estimated saturation fields. (b and g) Cartesian parameterization, (c and h) DCT-A parameterization, (d and i) DCT-B parameterization, (e and j) Structural Prior parameterization, (f and k) Gaussian Bell parameterization (see Figure 2 for details on the different parameterizations).

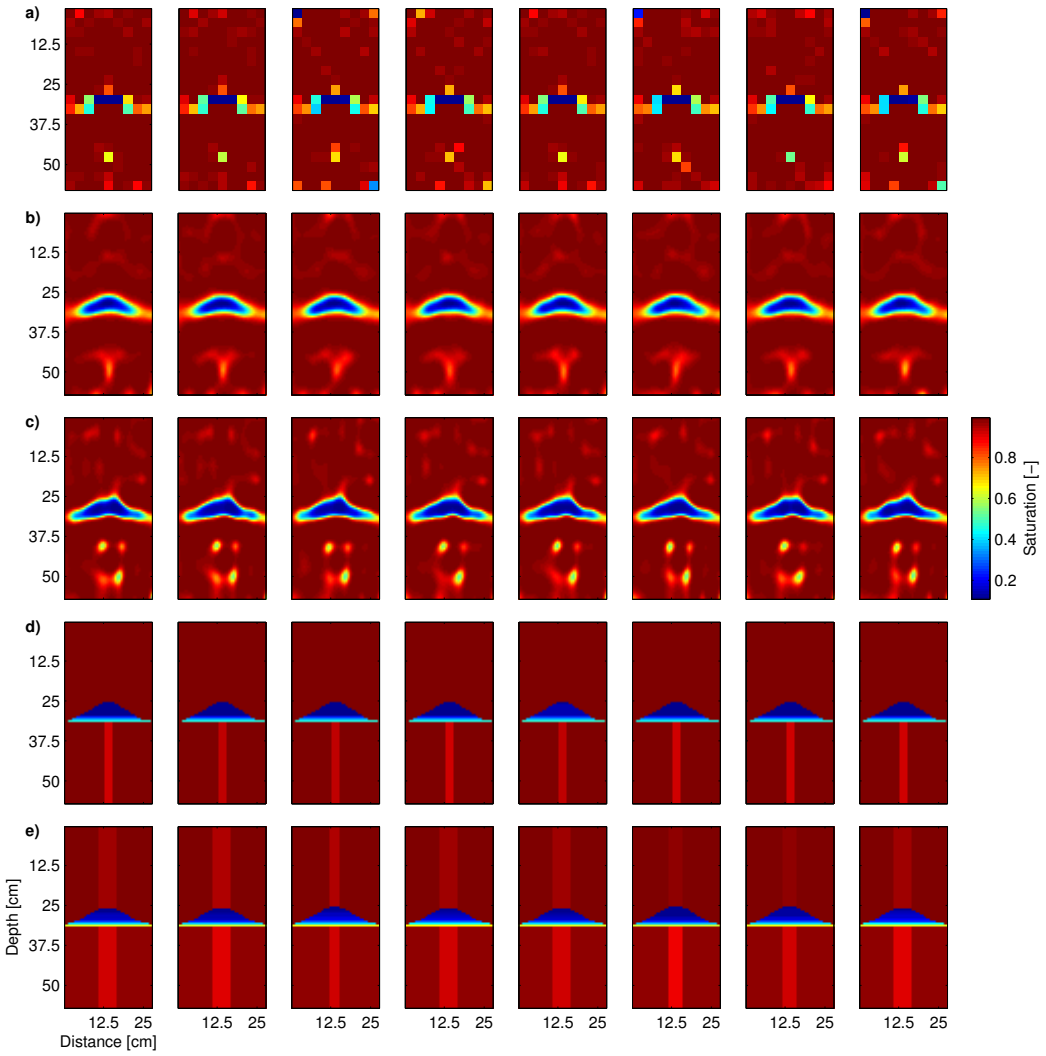

Figure 4: Saturation fields for the synthetic study: Random samples from the posterior pdf of the estimated saturation fields are shown for different parameterizations: a) Cartesian grid, b) DCT-A, c) DCT-B, d) Structural Prior parameterization, e) Gaussian Bell parameterization (see Figure 2 for details on the different parameterizations).

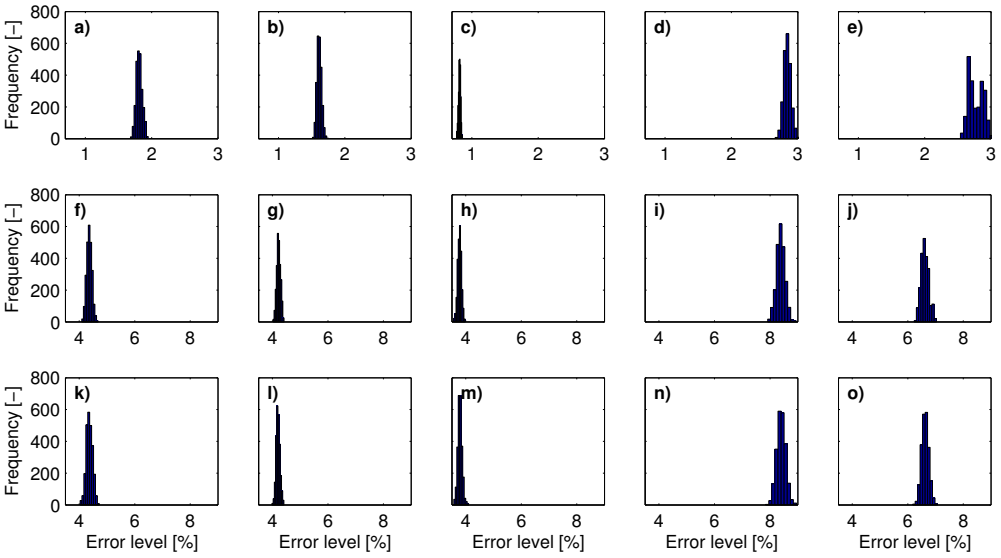

Figure 5: Error estimates for the different parameterization schemes and studies. (a-e) Synthetic study, (f-j) Real data study, (k-o) Real data study with gas volume constraint. Parameterizations from left to right: Cartesian grid, DCT-A, DCT-B, Structural Prior and Gaussian Bell.

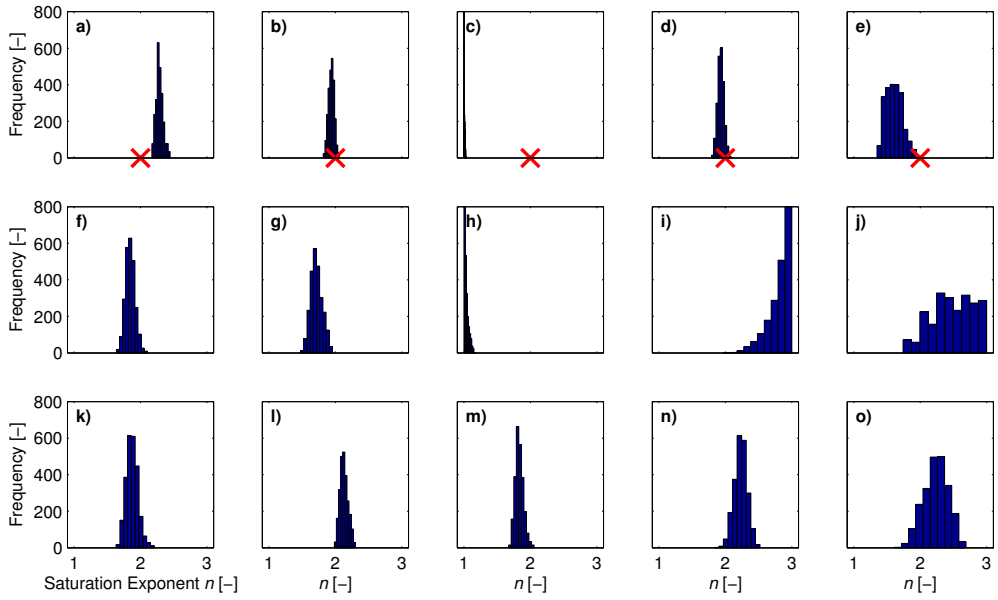

Figure 6: Estimated saturation exponents for the different parameterization schemes and studies. (a-e) Synthetic study, (f-j) Real data study, (k-o) Real data study with gas volume constraint. Parameterizations from left to right: Cartesian grid, DCT-A, DCT-B, Structural Prior and Gaussian Bell. For the synthetic study, the true saturation exponent is known (red crosses).

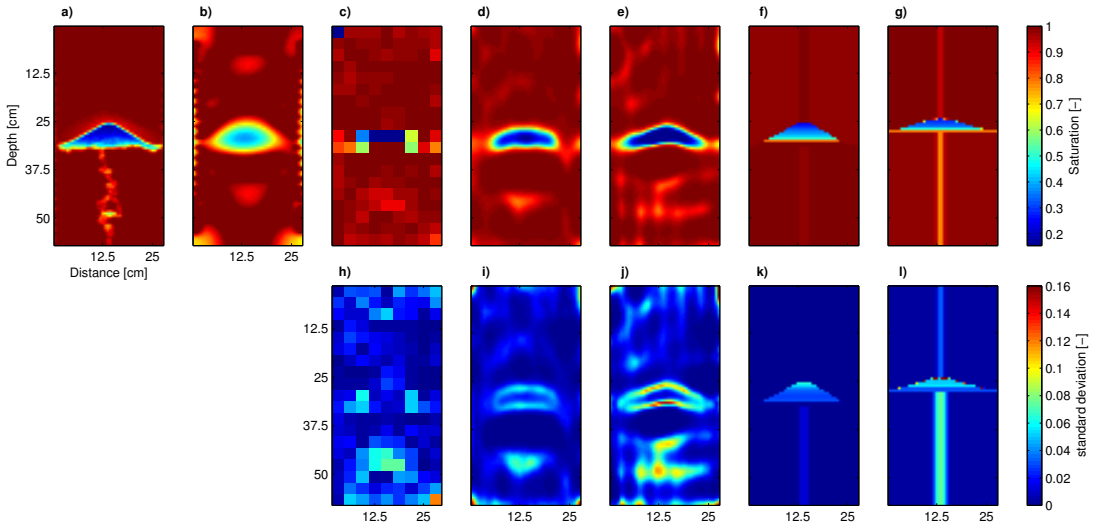

Figure 7: Saturation fields for the real data study: a) saturation from CCD imaging, b) saturation field estimated by Occam's inversion (from Figure 3 (top) of Breen et al., 2012). (c-g) Posterior mean saturation fields inferred from the MCMC inversion. (h-l) Standard deviations of the estimated saturation fields. (c and h) Cartesian parameterization, (d and i) DCT-A parameterization, (e and j) DCT-B parameterization, (f and k) Structural Prior parameterization, (g and l) Gaussian Bell parameterization (see Figure 2 for details on the different parameterizations).

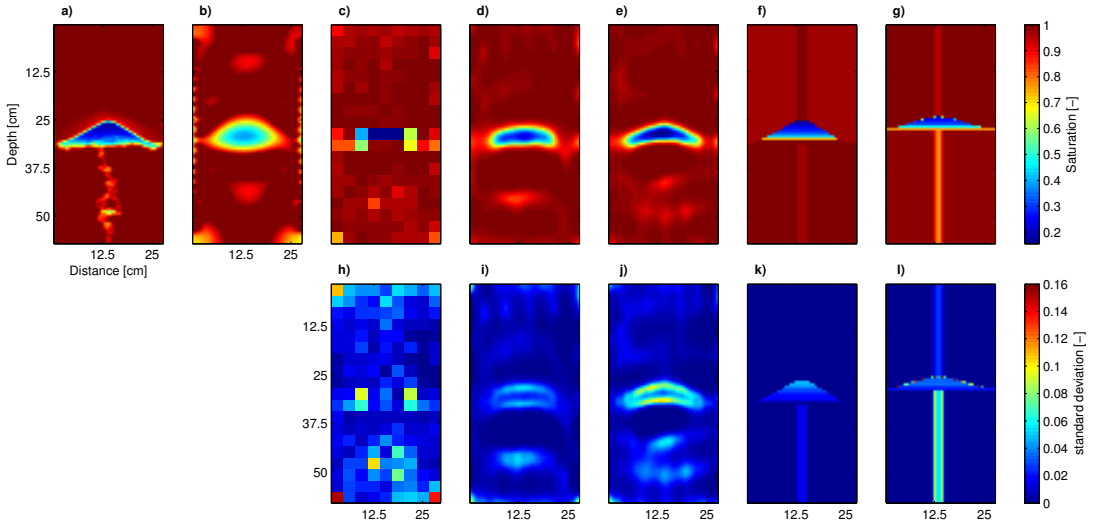

Figure 8: Saturation fields for the gas volume constrained real data study: a) Saturation from CCD imaging, b) saturation field estimated by Occam's inversion (from Figure 3 (top) of Breen et al., 2012). (c-g) Posterior mean saturation fields inferred from the MCMC inversion. (h-l) Standard deviations of the estimated saturation fields. (c and h) Cartesian parameterization, (d and i) DCT-A parameterization, (e and j) DCT-B parameterization, (f and k) Structural Prior parameterization, (g and l) Gaussian Bell parameterization (see Figure 2 for details on the different parameterizations).

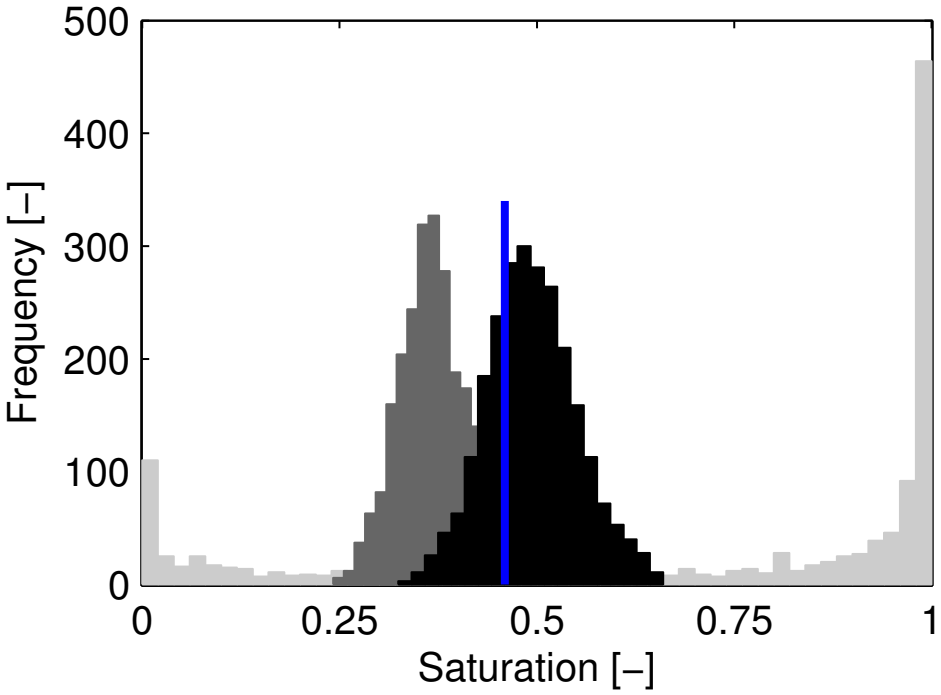

Figure 9: The effect of the gas volume constraint: Samples from the distribution of the saturation estimate in the center point of the model domain (for DCT-A parameterization and the real data study). Light gray: Prior (no ERT data, no constraints); dark gray: Posterior (ERT data, no constraints); black: Posterior (ERT data, gas volume constraint). The blue line depicts the saturation value from CCD imaging (Breen et al., 2012).

Table 1: Number of model parameters and required iterations to reach convergence for the synthetic study.

Parameterization	Parameters	Iterations ($\times 10^3$)
Cartesian Grid	174	235
DCT - A	103	90
DCT - B	108	100
Structural Prior	17	6
Gaussian Bell	22	37

Table 2: Saturation errors and estimates of total injected gas volume for the posterior saturation fields derived by MCMC inversion (true value: 28 ml).

Parameterization	Saturation error [-] mean ($\times 10^{-2}$)	std. dev. ($\times 10^{-3}$)	Gas volume estimate [ml] mean	std. dev.
Synthetic study				
Cartesian Grid	166.3	3.9	34.2	2.7
DCT - A	5.3	1.0	38.0	0.7
DCT - B	8.6	1.3	49.4	0.3
Structural Prior	5.5	0.5	29.8	0.5
Gaussian Bell	7.0	4.6	38.4	1.8
Real data w/o gas volume constraint				
Cartesian Grid	165.5	4.9	37.2	1.7
DCT - A	7.0	2.6	36.7	1.3
DCT - B	7.8	3.6	46.3	1.0
Structural Prior	9.8	1.6	21.2	1.2
Gaussian Bell	15.6	3.0	24.1	2.9
Real data with gas volume constraint				
Cartesian Grid	165.1	8.2	32.7	0.5
DCT - A	7.2	2.1	28.2	0.3
DCT - B	6.4	2.0	28.5	0.3
Structural Prior	9.5	1.1	27.9	0.3
Gaussian Bell	15.7	2.4	27.9	0.3